Genesis and Evolution of Surface Species during Pt Atomic Layer Deposition on Oxide Supports Characterized by in Situ XAFS Analysis and Water−Gas Shift Reaction

Worajit Setthapun,[†] W. Damion Williams,[‡] Seung Min Kim,[§] Hao Feng,[†] Jeffrey W. Elam,[||] Federico A. Rabuffetti,[⊥] Kenneth R. Poeppelmeier,[⊥] Peter C. Stair,[†,⊥] Eric A. Stach,[§] Fabio H. Ribeiro,[‡] Jeffrey T. Miller,[†] and Christopher L. Marshall*[,†]

Chemical Sciences and Engineering Division, Argonne National Laboratory, Argonne, Illinois 60439, Chemical Engineering, Purdue University, West Lafayette, Indiana 47907, Materials Engineering, Purdue University, West Lafayette, Indiana 47907, Energy Systems Division, Argonne National Laboratory, Argonne, Illinois 60439, and Department of Chemistry, Northwestern University, Evanston, Illinois 60208

Received: November 24, 2009; Revised Manuscript Received: March 15, 2010

Platinum atomic layer deposition (ALD) using $MeCpPtMe_3$ was employed to prepare high loadings of uniform-sized, 1−2 nm Pt nanoparticles on high surface area Al_2O_3, TiO_2, and $SrTiO_3$ supports. X-ray absorption fine structure was utilized to monitor the changes in the Pt species during each step of the synthesis. The temperature, precursor exposure time, treatment gas, and number of ALD cycles were found to affect the Pt particle size and density. Lower-temperature $MeCpPtMe_3$ adsorption yielded smaller particles due to reduced thermal decomposition. A 300 °C air treatment of the adsorbed $MeCpPtMe_3$ leads to PtO. In subsequent ALD cycles, the $MeCpPtMe_3$ reduces the PtO to metallic Pt in the ratio of one precursor molecule per PtO. A 200 °C H_2 treatment of the adsorbed $MeCpPtMe_3$ leads to the formation of 1−2 nm, metallic Pt nanoparticles. During subsequent ALD cycles, $MeCpPtMe_3$ adsorbs on the support, which, upon reduction, yields additional Pt nanoparticles with a minimal increase in size of the previously formed nanoparticles. The catalysts produced by ALD had identical water−gas shift reaction rates and reaction kinetics to those of Pt catalysts prepared by standard solution methods. ALD synthesis of catalytic nanoparticles is an attractive method for preparing novel model and practical catalysts.

1. Introduction

Metal oxide supported noble metal catalysts are ubiquitous in the automotive, chemical, and petroleum refining industries.[1] Because of the inherent high cost of noble metals, the ability to maximize their surface area by uniformly controlling their size, loading, and composition would reduce costs. Traditional catalyst synthesis techniques, including impregnation, ion-exchange, and deposition−precipitation, are effective in producing nanoparticles on the catalyst surface. However, these methods lack atomic-level control over the catalyst composition and surface structure and often yield relatively large metal clusters with a broad size distribution.[2]

Recently atomic layer deposition (ALD) has emerged as a promising, alternative technique with the ability to deposit uniform metal nanoparticles on catalyst supports.[3−6] This technique provides control of the active metal particle size and loading. This technique utilizes alternating, self-saturation chemical reactions between gaseous precursor molecules and a solid surface to deposit material in an atomic layer-by-layer fashion.[7] The four main steps in a single ALD cycle for noble metal deposition are (1) organometallic precursor adsorption, (2) inert gas purge, (3) precursor decomposition (in either air or hydrogen), and (4) inert gas purge. This cycle is typically repeated several times to reach the desired metal loading.

Much of the past work on noble metal ALD focused on microelectronic applications and consequently utilized hundreds of ALD cycles to prepare continuous, thin films.[7−9] Although it was recognized that the formation of continuous noble metal films by ALD proceeded via the coalescence of discrete islands, relatively few groups have focused on utilizing only the first few ALD cycles with the explicit intent of forming nanoparticles. Using this technique, Pt and Pd nanoparticle growth was observed on a variety of metal oxides.[3] Christensen and coworkers[10] also demonstrated that small and dispersed Pt nanoparticles were deposited on $SrTiO_3$(001). Platinum loading was found to increase linearly with the number of ALD cycles on $SrTiO_3$ nanocube supports.[4] This key finding suggests that ALD would be an excellent alternative method to deposit noble metal nanoparticles onto catalyst supports due to the ability to precisely control nanoparticle size and loading.

Besides these studies, there are only a few reports describing ALD for noble metal nanoparticle deposition. Catalysts consisting of Pt nanoparticles deposited on carbon and metal oxide supports were synthesized and found to be active for CO oxidation[5] and cinnamaldehyde hydrogenation.[11] Pt ALD has also been used to manufacture electrodes for proton-exchange membrane fuel cells.[6]

Insight into the mechanism for Pt ALD is provided by previous studies of Pt chemical vapor deposition (CVD). Xue et al.[12] studied Pt CVD from cyclopentadienyl trimethyl platinum ($CpPtMe_3$) and methylcyclopentadienyl trimethyl platinum ($MeCpPtMe_3$) in hydrogen. They reported that the initial heterogeneous decomposition of $CpPtMe_3$ is due to the electrophilic attack of

* To whom correspondence should be addressed. Tel: 1-630-252-4310. Fax: 1-630-972-4408. E-mail: Marshall@anl.gov.
[†] Chemical Sciences and Engineering Division, Argonne National Laboratory.
[‡] Chemical Engineering, Purdue University.
[§] Materials Engineering, Purdue University.
[||] Energy Systems Division, Argonne National Laboratory.
[⊥] Northwestern University.

10.1021/jp911178m
Published on Web 05/12/2010

the organometallic complex by surface hydroxyl groups present on both the glass and the Teflon substrates utilized in their experiments. Once deposited, the Pt catalyzed the further rapid decomposition of the organometallic complexes.[12] For Pt CVD with oxygen, Hiratani and co-workers[13] proposed the following pathway during the oxidative decomposition of $MeCpPtMe_3$:

$$Pt(s) + O_2(g) \rightarrow Pt{-}O_x \quad (1)$$

$$CH_3C_5H_4Pt(CH_3)_3 + Pt{-}O_x \rightarrow Pt(s) + CO_2(g) + H_2O(g) + \text{fragments} \quad (2)$$

Oxygen dissociatively adsorbs onto the Pt surface (eq 1). The ligands on the $MeCpPtMe_3$ precursor then react with adsorbed oxygen to form CO_2, H_2O, and hydrocarbon fragments (eq 2). The sequential chemistry proposed by Hiratani for Pt CVD motivated Aaltonen et al.[7] to suggest a similar mechanism for Pt ALD. The air exposure forms an adsorbed oxygen layer on the Pt surface. During the subsequent $MeCpPtMe_3$ exposure, some of the precursor ligands react with the adsorbed oxygen, yielding the gaseous products shown in eq 2. The limited supply of surface oxygen prevents all of the ligands from oxidizing and provides the self-limiting growth necessary for ALD. Complete oxidation occurs during the following O_2 exposure and forms a new adsorbed oxygen layer on the Pt. This mechanism is supported by quadrupole mass spectrometry (QMS) measurements in which CO_2 and H_2O were observed during both the $MeCpPtMe_3$ and the oxygen exposures.[14] Using infrared spectroscopy, Kessels et al.[15] found that one methyl group on average was liberated per $MeCpPtMe_3$ molecule during the Pt precursor exposures. Furthermore, Kessels discovered that approximately 50% of the methyl species was released as CH_4 formed by a ligand-exchange process in addition to the previously observed combustion products. These findings were corroborated by a recent study of Pt ALD using both in situ QMS and quartz crystal microbalance measurements.[16]

Although these previous studies form a fairly complete picture of Pt ALD on a preexisting Pt film, they do not yield any information about the mechanism for Pt particle formation on a metal oxide surface, nor do they describe the evolution of the Pt surface species during the precursor exposures and purge periods of the ALD process. In particular, these previous studies do not address the central question of when in the ALD cycle the reduction of the adsorbed Pt species to form metallic Pt actually occurs. In this work, X-ray absorption spectroscopy (XAFS) was utilized to directly probe the Pt surface species during each step of the ALD cycle. Platinum ALD was performed on high surface area powder substrates consisting of γ-Al_2O_3, Nanodur alumina, TiO_2, and $SrTiO_3$ by alternating exposures to $MeCpPtMe_3$ and either air or a hydrogen mixture. To our knowledge, this is the first application of in situ XAFS measurements to examine an ALD process. Knowledge gained from these detailed studies may lead to improved control over the loading and size of the metallic Pt nanoparticles, and this knowledge may extend to the synthesis of other metallic and multimetallic nanoparticles.

2. Experimental Methods

2.1. XANES and EXAFS Measurement and Analysis. X-ray absorption near edge structure (XANES) and extended X-ray absorption fine structure (EXAFS) measurements were conducted at the insertion-device beamline of the Materials Research Collaborative Access Team (MR-CAT) at the Advanced Photon Source located within the Argonne National Laboratory. The X-ray beam was calibrated to the Pt L3 edge. All XAFS measurements were taken in the transmission mode with ionization chambers optimized for the maximum current with linear response ($\sim 10^{10}$ photons detected/s). A cryogenically cooled double-crystal Si(111) monochromator with a resolution better than 2.5 eV at 11.564 keV (Pt L3 edge) was used with a Rh-coated mirror to minimize the presence of harmonics.

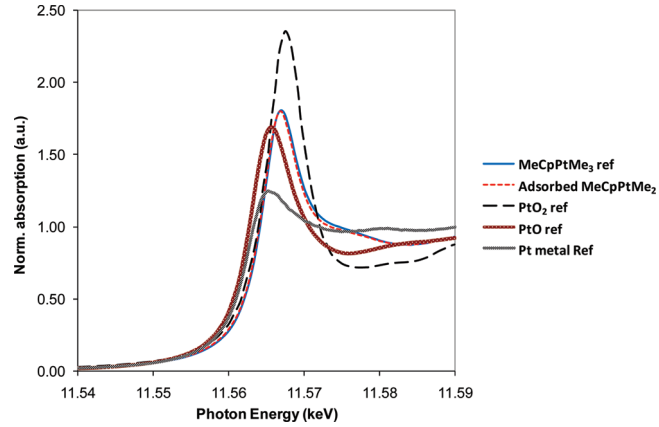

Figure 1. XANES reference spectra for $MeCpPtMe_3$, adsorbed $MeCpPtMe_2$, PtO_2, PtO, and metallic Pt.

WinXAS (version 3.1) and Athena (version 0.8.056) were used to fit XANES spectra for Pt fractions. The fitting method utilized linear combination fittings (LCF), and the error in XANES fittings was 10%. Appropriate XANES references were used for LCF. The references for metallic Pt (Pt^0), PtO, PtO_2, and $MeCpPtMe_3$ were measured at the beamline. For the Pt^0 XANES reference, a catalyst with a Pt particle size of $\sim$3 nm was reduced in 4%H_2/He at 250 °C. The spectra were taken of the reduced catalyst at room temperature in He. Platinum foil was not used as the Pt^0 XANES reference due to the differences in the Pt^0 spectrum for Pt foil and metallic Pt nanoparticles. Metallic Pt nanoparticle XANES has broader peaks than those of the Pt foil. The PtO and PtO_2 reference samples were finely ground and pressed into a pellet before collecting the XANES spectra. The $MeCpPtMe_3$ precursor was physically mixed with γ-Al_2O_3 and pressed into a pellet in the sample holder. The mixture sample holder was placed in a tightly sealed reactor that was transferred to the beamline where the XANES $MeCpPtMe_3$ reference spectrum was measured. The XANES spectra for $MeCpPtMe_3$ reference and the adsorbed precursor on the oxide support were almost identical (Figure 1). Because only a slight difference in the two XANES was observed, the XANES spectrum from the $MeCpPtMe_3$ precursor (nonadsorbed) was used to fit the catalyst samples. The adsorbed precursor on the oxide support will be referenced as "adsorbed $MeCpPtMe_2$".

The EXAFS analysis was also performed using WINXAS. Reference phase and amplitude files for Pt−Pt and Pt−O were taken from the Pt foil and the PtO EXAFS spectra. A single-shell model fit of the forward and inverse k^2-weighted EXAFS data was obtained between $k = 2.8-11.8$ Å^{-1} and $r = 1.3-3.0$ Å, respectively. An estimate of the particle size of Pt was made from the coordination number.[17] The EXAFS coordination number was shown to correlate with the Pt dispersion measured via hydrogen chemisorption using a 1:1 Pt/H ratio. The particle size was found to be inversely proportional to the dispersion. The Pt−Pt coordination number was used to determine fractions of surface atoms in the Pt nanoparticles (dispersion) and estimate the average size.

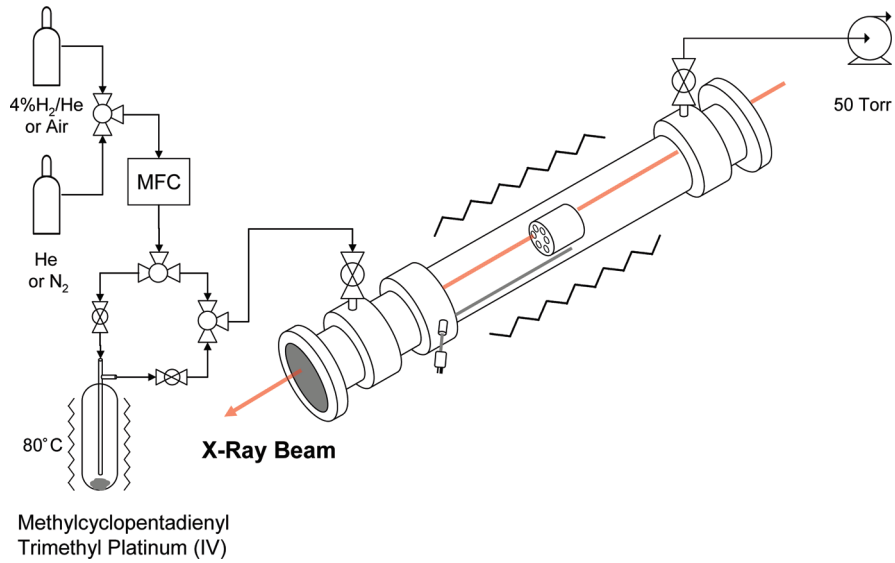

Figure 2. Continuous flow XAFS reactor system for Pt atomic layer deposition.

2.2. Pt ALD with in Situ XAFS Measurements. Platinum ALD over oxide supports was performed in a continuous-flow XAFS reactor. A schematic of the XAFS reactor system is shown in Figure 2. The reactor consisted of a straight quartz tube (1 in. OD, 10 in. length) with an Ultra-Torr fitting located on both ends. A seal was created by inserting aluminum windows (125 μm thick) into the Ultra-Torr fittings. A clam shell furnace was used to control the temperature of the reactor. All gas lines are $^1/_8$ in. stainless steel and heat traced to a temperature 10 °C above the Pt ALD exposure temperature. A vacuum pump connected to the reactor reduced the reactor pressure to 50 Torr. The ALD Pt precursor was methylcyclopentadienyl trimethyl platinum(IV) ($MeCpPtMe_3$) (Strem Chemicals). One gram of the precursor was loaded into the quartz saturator inside a glovebox. The saturator was then sealed and transferred to the ALD system.

Pt ALD was conducted over γ-Al_2O_3 (BASF, S.A. = 350 m^2/g), TiO_2 (BASF, S.A. = 220 m^2/g), and $SrTiO_3$ nanocubes (synthesized in-house, S.A. = 20 m^2/g)[18] in the continuous-flow XAFS reactor. These supports were gently pressed into a cylindrical sample holder containing six wells. The support thickness would give an absorbance (μx) of 1 in the Pt edge region (TiO_2, 10.5 mg; Al_2O_3, 19.9 mg; $SrTiO_3$ nanocubes, 12.4 mg). The sample holder was then placed in the center of the quartz reactor tube. The supports were degassed by heating to 150 °C under vacuum (50 Torr) in flowing ultra-high-purity N_2 at 60 mL/min for 15 min. The reactor was then cooled to 100 °C. In one experiment, four cycles of Pt ALD with O_2 treatment were conducted on the oxide supports. Each cycle was composed of four steps: (1) $MeCpPtMe_3$ exposure at 100 °C with N_2 (30 mL/min) carrier gas, (2) purge with N_2 (60 mL/min) at 100 and 300 °C, (3) oxidation with 20%O_2/N_2 (60 mL/min) at 300 °C, and (4) purge with N_2 (60 mL/min) at 300 °C. After the last step, the reactor was cooled to 100 °C to prepare for the next ALD cycle. During the $MeCpPtMe_3$ exposures, the saturator temperature was fixed at 80 °C to provide a $MeCpPtMe_3$ vapor pressure of 1.58 Torr.[12] In a separate experiment, three ALD cycles with H_2 treatment were performed. Each cycle consisted of (1) a Pt dose at 100 °C with He (30 mL/min) as carrier gas, (2) purge with He (60 mL/min) at 100 °C, (3) reduction with 4%H_2/He (180 mL/min) at 200 °C, and (4) purge with He (60 mL/min) at 200 °C and cool to 100 °C. XANES and EXAFS spectra were recorded after the completion of each step in the ALD cycle.

Additional time-dependent ALD experiments were performed on γ-Al_2O_3 with either O_2 or H_2 treatment. In these experiments, short XANES spectra (11 375−11 954 eV) were taken to monitor the changes in Pt species during the ALD process. The scan time was 1.3 min for these short spectra. After each ALD step, a few long scans (11 370−12 650 eV), which included both XANES and EXAFS sections, were also taken. In these experiments, a larger amount of γ-Al_2O_3 (80 mg) was gently pressed into a single sample holder with a 10 mm well diameter. Three Pt ALD cycles, as described previously, were carried out on the fresh support for either O_2 or H_2 treatments. The only difference from the experiments described above was that the first purging step was performed at 100 °C and then continued to either oxidation or reduction. Pt loadings on the γ-Al_2O_3 samples were determined using inductively coupled plasma optical emission spectrometry (ICP-OES) at Galbraith Laboratories, Inc. The absolute amounts of Pt in each species (μmol) during the ALD process were calculated by multiplying the Pt fraction, the edge step fraction, and the final Pt loading (μmol). The edge step fractions were calculated by dividing the edge step value from each spectrum by the final edge step of the last spectrum in the ALD process.

2.3. Synthesis of Pt ALD over Spherical Al_2O_3. Pt was deposited on spherical Al_2O_3 (sp-Al_2O_3) in a stainless steel viscous flow ALD reactor.[19] The sp-Al_2O_3 (NanoDur, Alfa Aesar) was nonporous and spherical, with a diameter of 40−50 nm and a surface area of 30−40 m^2/g. The sp-Al_2O_3 (0.5 g) was dispersed on a metal tray and installed into the reactor. Ultra-high-purity nitrogen (UHP N_2, Airgas, 99.999%) carrier gas continuously flowed at a mass flow rate of 60 mL/min and a pressure of 1 Torr. Pt ALD was performed by alternately exposing the support to $MeCpPtMe_3$ (Aldrich, 97%) and either oxygen or hydrogen for one to three ALD cycles. The $MeCpPtMe_3$ was held in a stainless steel bubbler maintained at 50 °C. During the Pt precursor exposures, 30 mL/min of N_2 was diverted through the bubbler, yielding a partial pressure of the Pt precursor in the ALD reactor of 0.1 Torr for 200 s, and the reactor temperature was maintained at either 100 or 300 °C. The O_2 or H_2 exposures were performed at 300 °C. The O_2 exposures used an O_2 mass flow rate of 30 mL/min for 200 s, whereas the H_2 exposures were 30 min at a total pressure of ~6 Torr. Between each reactant exposure, the reactor was continuously purged with UHP N_2 for 200 s.

2.4. Transmission Electron Microscopy. For transmission electron microscopy (TEM) investigation, catalyst samples were dispersed in ethanol and sonicated for 10 min. The solutions were then dropped on 200 mesh carbon-coated copper grids, and the grids were dried for 15 min at room temperature. All prepared samples were investigated using an 80−300 kV S/TEM FEI Titan.

2.5. Kinetic Measurements. The catalytic activity of the Pt/Al_2O_3 catalysts was investigated using a plug flow reactor apparatus, which has been described elsewhere.[20] For each experiment, 200−250 mg of the catalyst with a particle diameter size ranging between 0.12 and 0.25 mm was added to the reactor. Before the start of the water−gas shift experiments, the catalysts were reduced at 300 °C for 2 h with 50 mL/min of a 25% H_2/Ar mixture. After reduction, the catalysts were exposed to a standard water−gas shift composition of 6.8% CO, 8.5% CO_2, 21.9% H_2O, and 37.4% H_2, with the balance being Ar. This gas composition is meant to simulate that from a fuel reformer outlet. For all kinetic experiments, the total pressure was kept constant at ambient pressure with a total inlet flow rate of 75.4 mL/min. The catalysts were stabilized at approximately 300 °C under the standard gas composition for 20 h. During stabilization, the exit stream from the reactor was periodically injected into an Agilent 6890 gas chromatograph (GC). The inlet gases were analyzed before each injection to determine the response factors of the detectors and ensure precise measurements. The GC is equipped with a thermal conductivity detector and a Carboxen 1000 column operating with helium as a carrier gas.

After the stabilization process, the reactor temperature is adjusted to lower the CO conversion below 10% and maintain differential conditions during the kinetic measurements. Inclusion of the products in the kinetic measurements is done in order to achieve a differential reactor that has less than a 10% change in all gas concentrations. The rate of CO consumption was used as the net WGS rate under differential conditions. Turnover rates (TOR) are calculated using the dispersion of the metal, where it is assumed that the dispersion is inversely proportional to the average particle size (in nanometers). To determine the apparent activation energy, the temperature was varied over a range of 40 °C with the catalysts exposed to the standard gas concentrations. After the kinetic experiments were completed, the reactors were cooled to room temperature under flowing Ar. Once at room temperature, the catalysts were passivated by flowing a 1% O_2/Ar mixture for 1 h.

3. Results

3.1. Pt Loading with Increasing Number of ALD Cycles. $MeCpPtMe_3$ was adsorbed on γ-Al_2O_3, TiO_2, and $SrTiO_3$ at 100 °C, followed by air treatment at 300 °C. This procedure was repeated for four ALD cycles. For a given sample thickness, because the X-ray absorbance is proportional to the concentration, that is, the Beer−Lambert Law, the Pt edge step height is proportional to the amount of adsorbed Pt; see Figure 3a. The spectra show a constant increase in edge step height for each ALD cycle (Tables 1 and 2). A plot of the edge step normalized by the support surface area (Pt edge step/surface area of support) illustrates a linear increase in Pt loading for each support (Figure 3b). This is in agreement with the work of Christensen and co-workers,[4] who observed a linear increase in Pt loading of 4.4 wt % per cycle up to five ALD cycles on $SrTiO_3$ nanocubes. Although the absolute amounts of Pt adsorbed on TiO_2 and Al_2O_3 are very similar (Table 1), Figure 3b shows that the normalized edge step for γ-Al_2O_3 is lower than that for TiO_2.

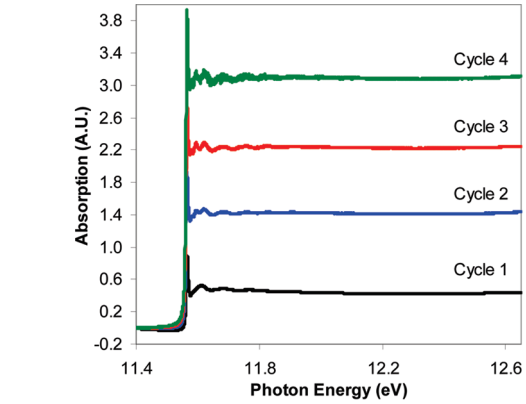

(a)

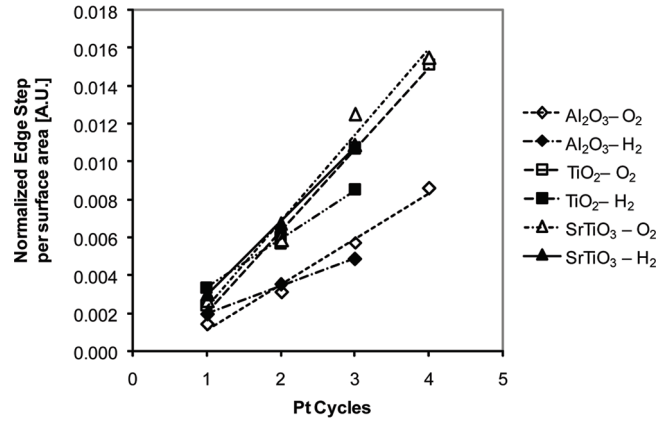

(b)

Figure 3. (a) XAFS spectra for Pt ALD cycles 1−4 over TiO_2 during N_2 purge after O_2 treatment. (b) Pt ALD cycles vs Pt edge step (normalized by support surface area) for Pt ALD over γ-Al_2O_3, TiO_2, and $SrTiO_3$ (open symbols represent ALD with O_2 treatment; closed symbols represent ALD with H_2 treatment).

This difference is due to the higher surface area of the γ-Al_2O_3 (350 m^2/g) compared with the TiO_2 (220 m^2/g). The 30 min $MeCpPtMe_3$ exposures were insufficient to fully cover the surface γ-Al_2O_3, resulting in a lower normalized step edge. The nearly identical normalized edge steps for TiO_2 and $SrTiO_3$ (20 m^2/g) suggest that these supports are nearly saturated during the 30 min $MeCpPtMe_3$ adsorption.

3.2. Determination of Supported Pt Species by XANES during ALD Synthesis Steps. ***3.2.1. 100 °C $MeCpPtMe_3$ Adsorption Followed by 300 °C Air Treatment.*** The shape and position of the XANES spectra were sufficiently different (Figure 1) to identify the Pt species on TiO_2, γ-Al_2O_3, and $SrTiO_3$ supports during the ALD synthesis steps. The results from XANES fittings are summarized in Table 1 for each step during the four ALD cycles where the adsorbed Pt is treated in air. Both TiO_2 and γ-Al_2O_3 have about 10 times higher surface areas, and therefore, have about 10 times more Pt deposited than $SrTiO_3$. The distributions of Pt species (i.e., metallic Pt, PtO, PtO_2, and adsorbed $MeCpPtMe_2$) were similar for TiO_2, γ-Al_2O_3, and $SrTiO_3$ during each of the four ALD cycles. After the initial $MeCpPtMe_3$ adsorption (cycle 1, step 1), approximately 90% of the supported Pt fraction was very similar in structure to the precursor and is likely chemisorbed $MeCpPtMe_2$. In addition, a small fraction of the precursor was reduced to metallic Pt. During the subsequent N_2 purge at 300 °C for 40 min, over 90% of the adsorbed Pt thermally decomposed to metallic Pt. Thermal decomposition of $MeCpPtMe_2$ was not expected because Aaltonen and co-workers[21] reported that

TABLE 1: Fractions of Pt Species and Pt Edge Step from XANES Spectra during Atomic Layer Deposition with O_2 Treatment

			TiO_2				γ-Al_2O_3					$SrTiO_3$			
Pt ALD cycle		ALD steps	Pt	PtO	MeCp $PtMe_2$	edge step	Pt	PtO	PtO_2	MeCp $PtMe_2$	edge step	Pt	PtO	MeCp $PtMe_2$	edge step
1	1	Pt dose and N_2 purge 100 °C	0.15		0.85	0.5	0.1			0.9	0.5	0.1		0.9	0.02
	2	N_2 purge 300 °C	1.0			0.5	0.9			0.1	0.5	0.95		0.05	0.05
	3	20% O_2/N_2 300 °C		1.0		0.5		0.8	0.2		0.5	0.05	0.95		0.05
	4	N_2 purge 100 °C		1.0		0.5		0.8	0.2		0.4	0.1	0.9		0.04
2	1	Pt dose and N_2 purge 100 °C	0.4	0.15	0.45	1.1	0.35	0.05		0.6	1.1	0.5		0.5	0.09
	2	N_2 purge 300 °C	1.0			1.3	1.0				1.2	0.95		0.05	0.15
	3	20% O_2/N_2 300 °C	0.05	0.95		1.4		1.0			1.3	0.45	0.55		0.15
	4	N_2 purge 100 °C	0.7	0.3		1.4	0.7	0.3			1.3	0.95	0.05		0.20
3	1	Pt dose and N_2 purge 100 °C	0.65	0.05	0.3	2.1	0.6	0.05		0.35	2.0	0.75		0.25	0.25
	2	N_2 purge 300 °C	1.0			2.2	0.95			0.05	2.1	1.0			0.24
4	1	Pt dose and N_2 purge 100 °C	0.75		0.25	3.0	0.7			0.3	3.0	0.75		0.25	0.31
	2	N_2 purge 300 °C	1.0			3.1		1.0			3.1	1.0		0	0.30

TABLE 2: Fractions of Pt Species and Pt Edge Step from XANES Spectra during Atomic Layer Deposition with H_2 Treatment

			TiO_2				γ-Al_2O_3				$SrTiO_3$			
Pt ALD cycle		ALD steps	Pt	PtO	MeCp $PtMe_2$	edge step	Pt	PtO	MeCp $PtMe_2$	edge step	Pt	PtO	MeCp $PtMe_2$	edge step
1	1	Pt dose and He purge 100 °C			1.0	0.7			1.0	0.7	0.1		0.9	0.06
	2	4%H_2/He 200 °C	0.95		0.05	0.7	0.9		0.1	0.7	0.9		0.1	0.05
	3	He purge 100 °C	0.8	0.2		0.7	0.7	0.3		0.7	0.4	0.6		0.06
2	1	Pt dose and He purge 100 °C	0.5	0.15	0.35	1.2	0.5		0.5	1.2	0.45		0.55	0.14
	2	4%H_2/He 200 °C	0.95		0.05	1.2	0.95		0.05	1.2	0.95		0.05	0.14
	3	He purge 100 °C	0.95	0.05		1.2	0.85	0.15		1.2	0.65	0.35		0.14
3	1	Pt dose and He purge 100 °C	0.6	0.1	0.3	1.7	0.65	0.05	0.3	1.7	0.6		0.4	0.21
	2	4%H_2/He 200 °C	0.95		0.05	1.7	0.85	0.05	0.1	1.7	0.95		0.05	0.21
	3	He purge 100 °C	1.0			1.7	0.95	0.05		1.7	0.9	0.1		0.21

decomposition occurred in the presence of O_2 and not during the purging step in Pt ALD at 300 °C. The N_2 purging periods at 300 °C utilized in our study provide sufficient time for the adsorbed precursor to completely decompose. The purging period in a conventional ALD process lasts only a few seconds, and consequently, decomposition is not typically observed. Air treatment at 300 °C (step 3) oxidized all of the metallic Pt and the remaining adsorbed Pt precursor to Pt oxides. The Pt species on TiO_2 and $SrTiO_3$ were converted completely to PtO; however, on γ-Al_2O_3, there was a mixture of PtO (0.80) and PtO_2 (0.20). The Pt oxides on all three supports remained unchanged as the reactor was cooled to 100 °C under a flow of N_2 in preparation for the next Pt exposure in the second ALD cycle.

In the second ALD cycle, the Pt loading increased by approximately the same amount as during the first ALD cycle for each support. This increase was due to newly adsorbed $MeCpPtMe_2$, as indicated by the Pt fraction of approximately 50%. In addition, new precursor adsorption reduced the PtO (from oxidation in first cycle) to metallic Pt. This reduction is likely caused by the organic precursor ligands. Complete reduction of PtO occurred only on $SrTiO_3$, while small amounts (10−30%) of the initial PtO remained on TiO_2 and γ-Al_2O_3. After heating the catalyst to 300 °C in N_2 for 40 min, the adsorbed $MeCpPtMe_2$ again decomposed to metallic Pt. Similar to cycle 1, oxidation during the second cycle led to PtO for TiO_2 and γ-Al_2O_3. However, on $SrTiO_3$, 45% of the Pt remained metallic. During cooling in N_2 prior to beginning the third ALD cycle, a large fraction of the oxidized PtO was reduced to metallic Pt. For TiO_2 and γ-Al_2O_3, approximately 70% of the Pt became metallic, whereas on $SrTiO_3$, about 95% of the Pt became metallic. It is possible that residual $MeCpPtMe_3$ in the transfer line was responsible for this reduction because a small increase in edge step height was observed during the cooling and reduction steps.

After the third $MeCpPtMe_3$ exposure, approximately $^1/_3$ of the Pt consisted of adsorbed $MeCpPtMe_2$, while the remainder was metallic Pt. Similar to the second ALD cycle, the addition of $MeCpPtMe_2$ reduced the PtO. As seen in the previous cycles, heating to 300 °C decomposed all of the adsorbed $MeCpPtMe_2$ to metallic Pt. With each ALD cycle, oxidation of the Pt appeared to have no effect on the subsequent amount of Pt adsorption. Thus, during the third and fourth ALD cycle, the oxidation step was omitted. After the fourth Pt exposure, ~25% of the Pt was present as adsorbed $MeCpPtMe_2$, while the remainder was metallic Pt. Similar to the previous cycles, the Pt precursors decomposed to metallic Pt when heated to 300 °C under N_2.

During the previous experiments, XANES spectra were recorded only after completion of each treatment step. To better understand the Pt synthesis, the Pt ALD was repeated and XANES spectra were recorded every 1.3 min, allowing the time evolution of each surface species to be monitored during each synthesis step. The results of the XANES fits are presented in Figure 4. The relative Pt fractions as a function of time are illustrated in Figure 4a, whereas the absolute amounts of each Pt species are shown in Figure 4b. The proposed models for Pt ALD on metal oxide surfaces are illustrated in Figure 4c. For the first cycle Pt deposition, about 85% of the Pt was adsorbed as $MeCpPtMe_2$ and 15% as PtO (Figure 4a). This result is slightly different from the previous experiments where, after the first Pt dose, 90% was $MeCpPtMe_2$ and 10% was metallic Pt. In this experiment, a small amount of O_2 contamination may have oxidized the metallic Pt. During the adsorption step, the Pt loading increased linearly, while the amount of PtO remained constant. The adsorbed $MeCpPtMe_2$ was subsequently treated in air at 100, 200, and 300 °C. As shown in Figure 4a, the rate of oxidation increased with increasing temperature and the oxidation to PtO was complete at 300 °C.

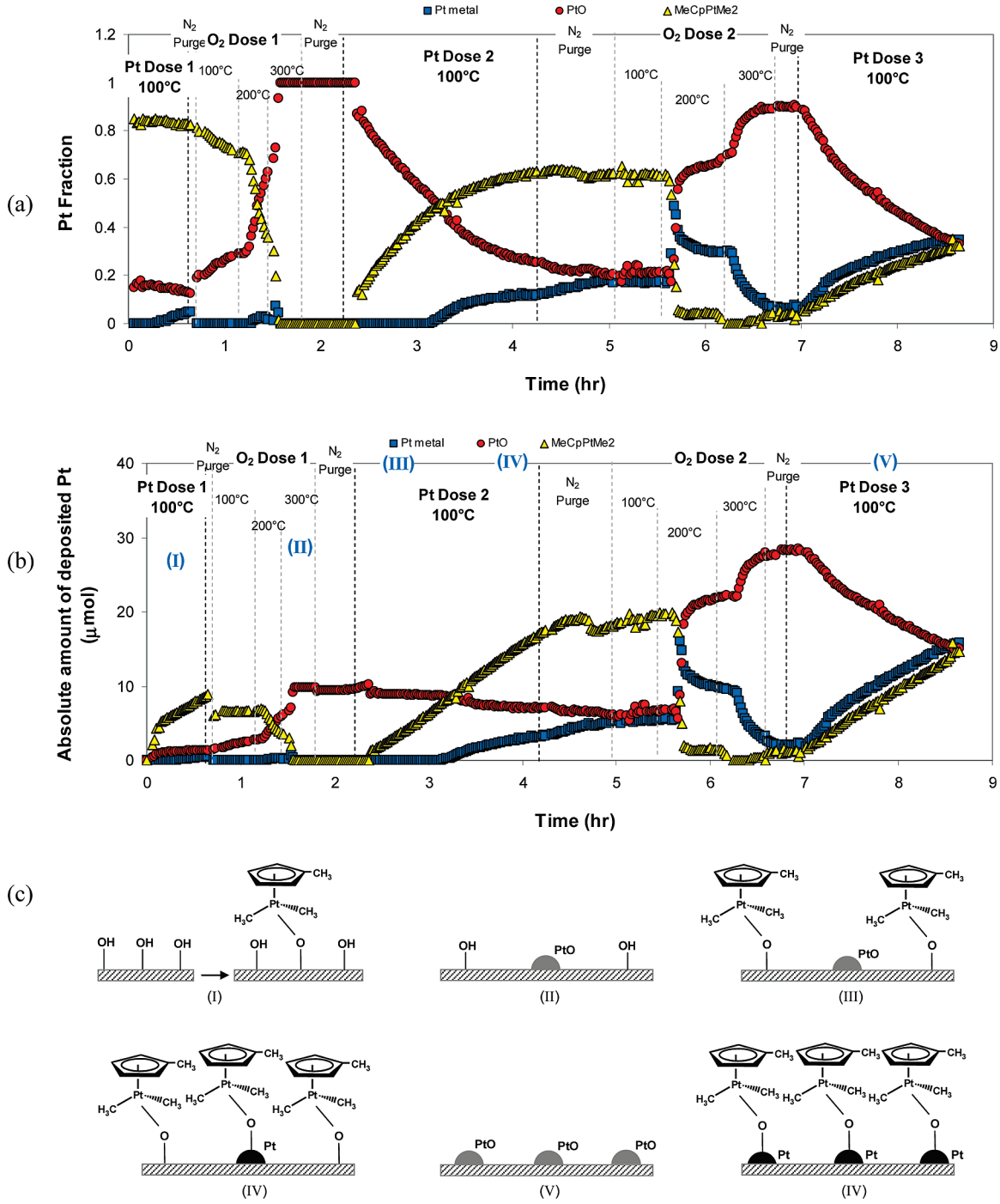

Figure 4. (a) Pt fractions from XANES fits for metallic Pt, PtO, and adsorbed $MeCpPtMe_2$. (b) Absolute amount of each Pt species. (c) Proposed schemes during three cycles of Pt ALD with O_2 treatment on γ-Al_2O_3.

During the second cycle of Pt addition (100 °C in N_2), there was again a linear increase in the amount of adsorbed $MeCpPtMe_2$ and the amount of PtO remained constant (Figure 4b, (III)). The fraction of PtO decreased due to an increase of the total Pt loading (Figure 4a). After approximately 1 h, the amount of adsorbed precursor continued to increase, however, at a reduced rate. During this second hour, the PtO also began to reduce to metallic Pt (Figure 4b, (IV)). This result suggests that, initially, the $MeCpPtMe_3$ reacts with the support hydroxyl groups, rather than oxidized Pt. Once there are few available support sites, the precursor begins to reduce with PtO to Pt nanoparticles. While no oxidative decomposition was observed at 100 °C, initially, at 200 °C, there is a rapid decrease in the amount of adsorbed $MeCpPtMe_2$ and an increase in the amount of metallic Pt. At longer times, the metallic Pt is oxidized to PtO, and at 300 °C in air, all the Pt is oxidized to PtO.

During the third ALD cycle, the adsorption of $MeCpPtMe_3$ increased approximately linearly, but the fraction of previously adsorbed PtO fractions decreased from the beginning with an increase in the fraction of metallic Pt. The loss in the amount of PtO (14 μmol) is virtually equivalent to the gain in metallic Pt (13 μmol) and also equivalent to the amount of adsorbed $MeCpPtMe_2$ (13 μmol) (Figure 4b, (VI)). This equivalency suggests that each $MeCpPtMe_3$ molecule reacts with and reduces one PtO unit, yielding one atom of metallic Pt. The reduction of PtO by the precursor only occurs at high surface coverage of Pt, that is, during the second hour of cycle 2 or immediately during cycle 3.

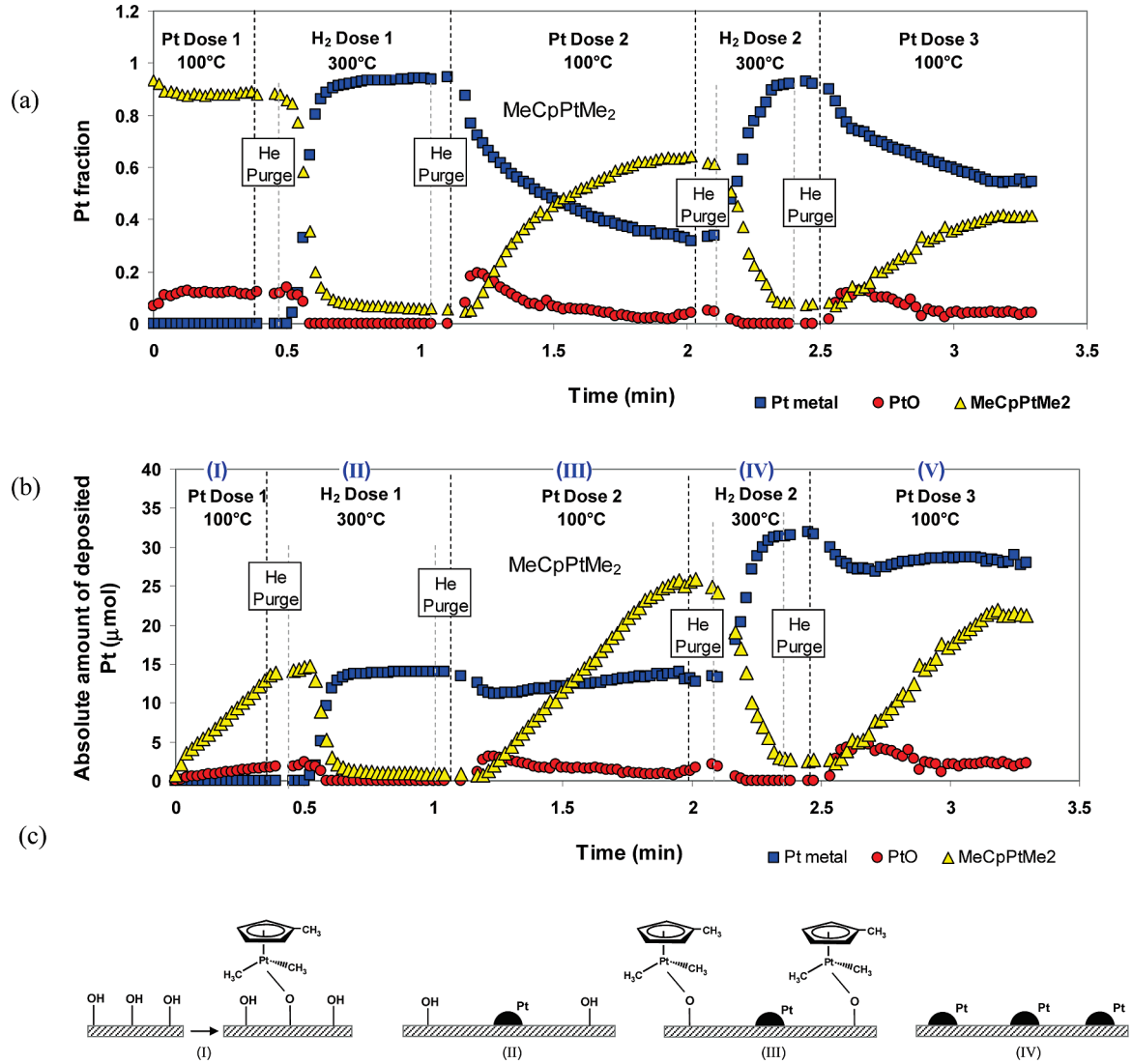

Figure 5. (a) Pt fractions from XANES fits for metallic Pt, PtO, and adsorbed $MeCpPtMe_2$. (b) Absolute amount of each Pt species. (c) Proposed schemes during three cycles of Pt ALD with H_2 treatment on γ-Al_2O_3.

3.2.2. 100 °C MeCpPtMe$_3$ Adsorption Followed by 200 °C H$_2$ Treatment. The Pt species observed on the TiO_2, γ-Al_2O_3, and $SrTiO_3$ supports using XANES spectroscopy during three cycles of $MeCpPtMe_3$ adsorption and subsequent H_2 treatment are summarized in Table 2. The fractions of Pt species were relatively similar for all three supports and all three ALD cycles. The XANES spectrum recorded following the $MeCpPtMe_3$ exposure is very similar to that of the precursor, consistent with adsorbed $MeCpPtMe_2$ species. As discussed above, because a long N_2 purge at 300 °C leads to thermal decomposition of the adsorbed $MeCpPtMe_2$, the purge for H_2 treatment was conducted at 100 °C. Subsequent treatment with 4% H_2/He was conducted at 100, 200, and 300 °C. At 200 °C, the adsorbed Pt precursor was fully reduced to Pt nanoparticles. On all three supports, the metallic Pt fraction represents more than 90% of the total Pt. Therefore, a reduction temperature of 200 °C was chosen for the remaining ALD cycles. After reduction, the catalyst was purged in He and cooled to 100 °C. During the cooling step, the metallic Pt was partially oxidized to PtO. $SrTiO_3$ has a PtO fraction of 60%, whereas TiO_2 and γ-Al_2O_3 have PtO fractions of 20 and 30%, respectively. The partial oxidation is likely due to a small air leak into the reactor (operating under a dynamic vacuum of roughly 50 Torr) or from contaminants in the He cylinder.

During the second Pt adsorption step (30 min), 50% of the Pt fraction was adsorbed as $MeCpPtMe_2$ and the remainder was metallic Pt for γ-Al_2O_3 and $SrTiO_3$. On TiO_2, however, not all of the PtO was reduced to metallic Pt. Again, H_2 treatment at 200 °C caused complete reduction to metallic nanoparticles. As before, upon switching to N_2, small amounts of Pt were oxidized on all supports. TiO_2, γ-Al_2O_3, and $SrTiO_3$ had PtO fractions of 5, 15, and 35%, respectively. The third ALD cycle again led to adsorbed precursor in amounts similar to the first two ALD cycles, and the PtO (from the second cycle) was reduced to metallic Pt. As observed in the other cycles, the adsorbed $MeCpPtMe_2$ was reduced to metallic nanoparticles at 200 °C.

Time-dependent XANES measurements were performed during three ALD cycles using H_2 treatment with the γ-Al_2O_3 support. Figure 5a,b illustrates the relative fraction and absolute amounts of Pt species during the individual steps, and Figure 5c shows the proposed model. The rate of Pt deposition was constant during the initial $MeCpPtMe_3$ exposure. Approximately 90% of the Pt was adsorbed $MeCpPtMe_2$ with a small amount of PtO that also increased during the $MeCpPtMe_3$ exposure. During the previous experiments, PtO was not observed (Table 2), suggesting a small air leak during these time-dependent experiments. Exposure to H_2 at 300 °C leads to ~90% reduced Pt and ~10% PtO. During the second ALD cycle, the metallic

TABLE 3: EXAFS Fitting Results for Coordination Number (CN), Bond Distance (R), Debye−Waller Factor (DWF), and Energy Correction Factor (E_0) for Each Cycle of Pt ALD over TiO_2, γ-Al_2O_3, and $SrTiO_3$ with O_2 and H_2 Treatment

			ALD O_2 (N_2 at 300 °C)					ALD H_2 (4%H_2/He at 200 °C)				
support	cycle	scatter	size (nm)	CN	R (Å)	DWF × 10^{-3}	E_0	size (nm)	CN	R (Å)	DWF × 10^{-3}	E_0
TiO_2	1	Pt−Pt	1.1	4.8	2.65	7	−5	1.5	5.8	2.66	6	−6.1
	2	Pt−Pt	1.3	5.3	2.68	7	−2.7	1.6	5.9	2.67	6	−5.6
	3	Pt−Pt	1.8	6.3	2.69	7	−2.9	1.5	5.8	2.68	6	−5.5
	4	Pt−Pt	2.1	6.8	2.71	7	0.6					
γ-Al_2O_3	1	Pt−Pt	1.5	5.8	2.62	7	−7.6	1.1	4.1	2.63	6	−7.8
	2	Pt−Pt	1.2	4.9	2.65	7	−5.7	1.4	5.2	2.66	6	−5.9
	3	Pt−Pt	1.5	5.6	2.67	7	−4.2	1.5	5.7	2.66	6	−5.5
	4	Pt−Pt	1.5	5.6	2.69	7	−4					
$SrTiO_3$	1	Pt−Pt										
	2	Pt−Pt	1.8	6.3	2.65	7	−5.7	0.8	3.8	2.73	6	−1.2
	3	Pt−Pt	2.4	7.3	2.70	7	−3.4	1.1	4.8	2.70	6	−3.5
	4	Pt−Pt	3.0	8.0	2.72	7	−1.9					

Pt fraction decreased from 90% to 30% due to dilution by the newly adsorbed Pt, while the fraction of $MeCpPtMe_2$ increased from 0 to 65%. The second cycle of $MeCpPtMe_3$ exposure lasted approximately 1 h, and at the end of this period, the amount adsorbed appeared to level off. Initially, the fraction of PtO increased slightly to 20% during the first 10 min but decreased to near 0% at the end of the $MeCpPtMe_3$ exposure. In Figure 5b, the amount of metallic Pt slightly decreased in the first 10 min but slowly increased and became constant throughout the $MeCpPtMe_3$ exposure. The absolute amounts of Pt and PtO during the $MeCpPtMe_3$ exposures of cycles 2 and 3 exhibit an inverse correlation (Figure 5b). This finding suggests that the PtO is reduced by the $MeCpPtMe_3$ to form metallic Pt; however, no additional metallic Pt is formed during the $MeCpPtMe_3$ exposures. During the third $MeCpPtMe_3$ exposure, additional precursor adsorbs onto the support; however, the increase in loading begins to level off after about 30 min. Again, a small amount of oxidized Pt is initially formed during the $MeCpPtMe_3$ exposure, which decreases upon further exposure to the Pt precursor.

3.3. EXAFS Analysis and TEM Images. Although XANES measurements can identify the adsorbed Pt species and quantify their surface concentrations, EXAFS can provide structural details about the adsorbed Pt. A summary of the EXAFS fitting for Pt on the TiO_2, γ-Al_2O_3, and $SrTiO_3$ substrates is presented in Table 3. For the ALD performed using air treatment, EXAFS measurements were collected after 1 h of N_2 purging at 300 °C. For samples prepared using H_2 treatment, the spectra were measured during H_2 reduction at 200 °C. In the EXAFS fits, the Debye−Waller factor (DWF) is temperature-dependent. The DWF was determined by fitting the EXAFS spectra at both 300 °C and room temperature for the same sample. To determine the DWF value at 300 °C, the coordination number at room temperature was used in the fit. Because the temperature dependence of the DWF is linear, the DWF at any temperature can be calculated and fixed in the fit at high temperature.[22] DWFs of 0.007 and 0.006 were used for EXAFS fitting at 300 and 200 °C, respectively.

The EXAFS fits in Table 3 indicate the formation of small, metallic Pt particles, as evident from the low Pt−Pt coordination numbers and the strongly contracted bond distances.[17,22] A fully coordinated shell in Pt metal has 12 nearest-neighbor Pt atoms with a bond distance of 2.77 Å. However, our results for the various supports indicate that the coordination numbers and bond distances were in the range of 4.1−8.0 and 2.62−2.72 Å, respectively. High loadings of 1−2 nm Pt nanoparticles are formed by decomposition of the low-temperature, adsorbed $MeCpPtMe_3$ precursor in H_2 or N_2. In addition, oxidation of the Pt nanoparticles at 300 °C had a minor effect on the particle size in subsequent ALD cycles.

The EXAFS results for TiO_2 indicated that the Pt−Pt coordination number gradually increased from 4.8 to 6.8 between one and four ALD cycles using O_2 treatment. Therefore, the Pt particle size slightly increased from 1.1 to 2.1 nm. The Pt−Pt bond distances also increased from 2.65 to 2.71 Å. With H_2 treatment, however, the Pt particle size remained approximately constant at 1.5 nm for one to three cycles of ALD, even though there was a large increase in Pt loading. For γ-Al_2O_3, the Pt particle size also remained constant at ∼1.5 nm through all four ALD cycles using O_2 treatment. With the H_2 treatment, the Pt particle size slightly increased from 1.1 to 1.5 nm. For $SrTiO_3$, the ALD cycle 1 EXAFS data could not be fit because the edge step and signal-to-noise were too small. On $SrTiO_3$, the Pt particles were larger than on TiO_2 and Al_2O_3 and increased in size with increasing ALD cycles using both the O_2 and the H_2 treatments. The Pt nanoparticles deposited onto the $SrTiO_3$ were larger using the O_2 treatment than the H_2 treatment.

Because EXAFS yields only the average Pt particle size, TEM was used to evaluate the particle size distribution. Figure 6a,b shows TEM images of TiO_2 following one and four Pt ALD cycles, respectively, using the O_2 treatment. For both samples, the Pt nanoparticles are all in the range of ∼1 to 2 nm, yielding a very narrow size distribution. The Pt particle density increased significantly following four ALD cycles, yet the average particle size and size distribution remained nearly constant. In contrast, Figure 6c,d demonstrates an increase in Pt particle size on $SrTiO_3$ from ∼3 to 7 nm between one and four ALD cycles with O_2 treatment. Figure 7 shows TEM images recorded following three ALD cycles using H_2 on TiO_2 (Figure 7a) and $SrTiO_3$ (Figure 7b). Similar to the TEM images in Figure 6, the Pt particle size distribution is very narrow (±1 nm) for the samples prepared using the H_2 treatment. The TEM images of ALD Pt on γ-Al_2O_3 exhibited poor contrast and are not shown.

3.4. TEM Analysis of Pt on Spherical Al_2O_3. In contrast to the amorphous γ-Al_2O_3 support, Pt nanoparticles on spherical Al_2O_3 (sp-Al_2O_3) yielded high-contrast TEM images, allowing accurate evaluation of the Pt particle size. A series of samples were prepared on spherical alumina using $MeCpPtMe_3$ adsorption at 300 °C, short N_2 purge periods, and air treatment at 300 °C. TEM images of the samples formed using one to three ALD cycles, Pt/sp-Al_2O_3, are shown in Figure 8a−c. The Pt particle sizes following one, two, and three ALD cycles are 2.3 ± 0.3, 2.7 ± 0.5, and 2.9 ± 0.5 nm, respectively, and are evenly distributed across the support.

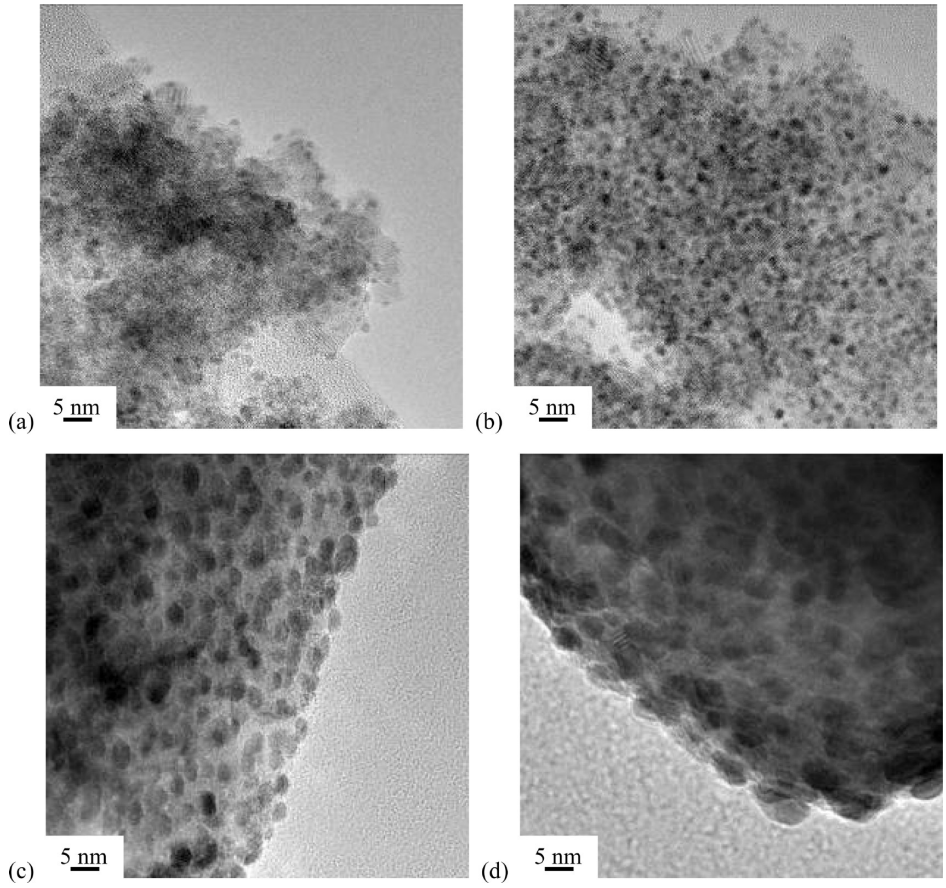

Figure 6. TEM images of (a) 1cPt/TiO_2, (b) 4cPt/TiO_2, (c) 1cPt/$SrTiO_3$, and (d) 4cPt/$SrTiO_3$ synthesized in situ in the XAFS reactor with O_2 treatment.

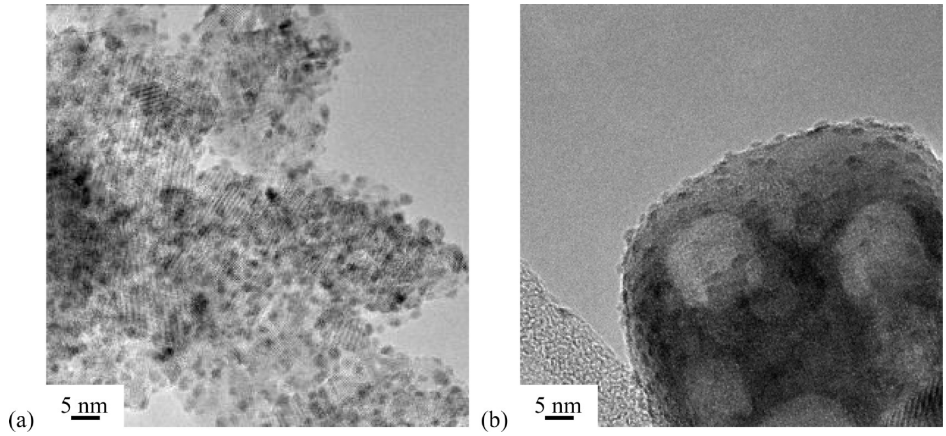

Figure 7. TEM images of (a) 3cPt/TiO_2 and (b) 3cPt/$SrTiO_3$ synthesized in situ in the XAFS reactor with H_2 treatment.

3.5. WGS Kinetics of Pt/sp-Al_2O_3 Catalysts. The catalytic properties of the ALD nanoparticles were determined for the water−gas shift reaction (WGS). Results of the kinetic experiments performed on the Pt/sp-Al_2O_3 catalysts are summarized in Table 5. The apparent activation energies for the three Pt/sp-Al_2O_3 catalysts range between 80 and 89 kJ/mol. With increasing Pt loading, the reaction rate at 270 °C was equal to 1.7, 1.9, and 2.5 μmol of CO per gram of catalyst per second at the standard test conditions. When changes in the weight loading and dispersion of Pt are taken into account, the TOR for the 1cPt/sp-Al_2O_3 catalyst was the highest of the three Pt/sp-Al_2O_3 catalysts studied. Furthermore, the WGS TOR at 270 °C decreased as more cycles of Pt were added to the sp-Al_2O_3 support.

3.6. Platinum Particle Stability. All three Pt/sp-Al_2O_3 catalysts had an initial deactivation within the first 400 min of the WGS reaction. The lined out rate was between 80 and 90% of the initial recorded rate (Figure 9). After this initial deactivation, the WGS rates were stable for the remainder of the 20 h on stream. Analysis of the Pt particle size after WGS reaction by TEM indicates that the particle size increased; see Figure 8d−f. The changes in the average particle size were less than approximately 1 nm and indicate that the size of the platinum on the low surface area sp-Al_2O_3 is relatively stable even at high loadings under WGS conditions. The estimated Pt dispersion on the used catalysts was used to calculate the lined out turnover rate (TOR), that is, the rate per surface atom.

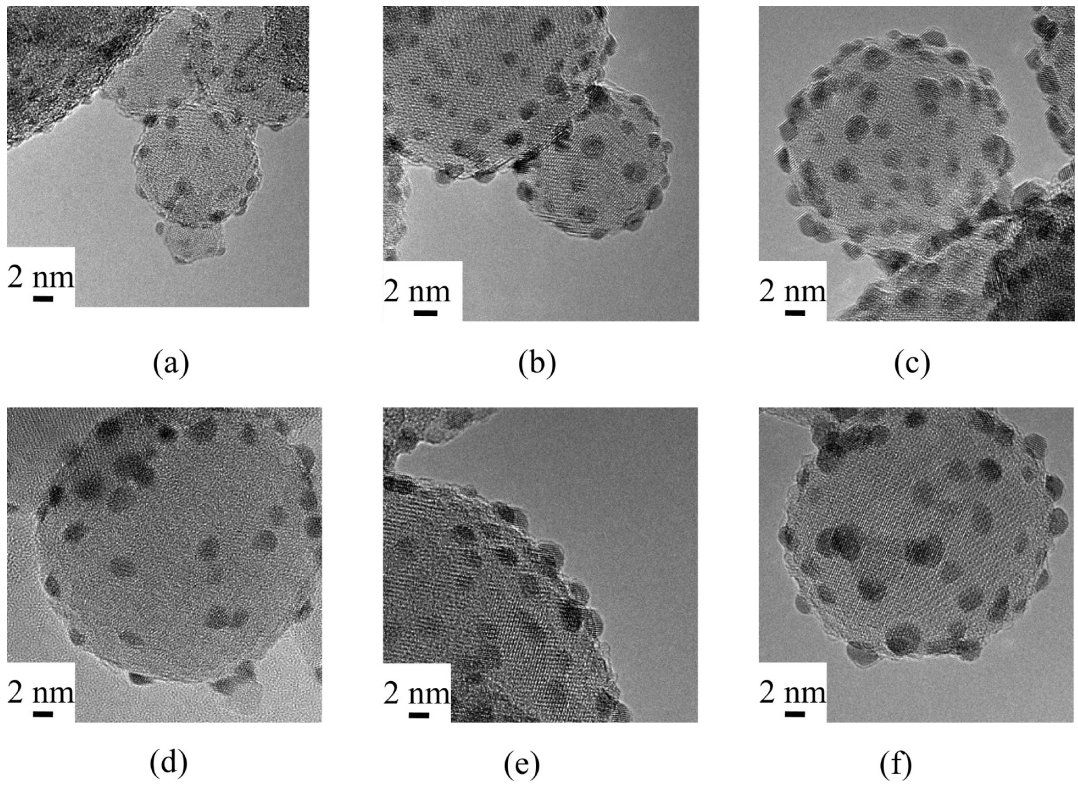

Figure 8. TEM images of one to three cycles of Pt ALD at 300 °C on sp-Al_2O_3 with O_2 treatment. As prepared: (a) one cycle Pt, (b) two cycles Pt, and (c) three cycles Pt. After WGS: (d) one cycle Pt, (e) two cycles Pt, and (f) three cycles Pt.

TABLE 4: EXAFS Fitting during O_2 Dose at 300°C

support	cycle	scatter	CN	R (Å)	DWF × 10^{-3}	E_0
TiO_2	1	Pt−O	4	2.04	4	0.2
	2	Pt−O	3.8	2.03	4	−0.3
γ-Al_2O_3	1	Pt−O	4.2	2.04	4	0.1
	2	Pt−O	4.3	2.03	4	−0.5

TABLE 5: Water−Gas Shift Kinetics

catalyst	loading wt %	dispersion	E_a (kJ mol^{-1})	T^c (°C)	TOR^d (× 10^{-3} s^{-1})	ref
1cPt/sp-Al_2O_3	2.5	0.32[a]	89	250−290	13.0	this work
2cPt/sp-Al_2O_3	6.5	0.29[a]	86	250−290	5.7	this work
3cPt/sp-Al_2O_3	10.4	0.28[a]	80	250−290	4.6	this work
Pt/γ-Al_2O_3	1.0	0.47[b]	68	225−285	12.4	[35]
Pt/γ-Al_2O_3	3.0	0.31[b]	71	250−300	29.8	[36]

[a] Dispersion calculated from TEM average particle size after reaction. [b] Dispersion calculated from chemisorption experiments. [c] Temperature range over which the activation energy was determined. [d] Rates calculated at 270 °C and 6.8% CO, 21.9% H_2O, 8.5% CO_2, and 37.4% H_2, with the balance being Ar.

4. Discussion

4.1. ALD Temperature. Pt ALD is typically performed at a constant temperature.[3,4,6,7,21,23] Aaltonen and co-workers[7] proposed an optimal temperature of 300 °C with $MeCpPtMe_3$ exposure times of 0.2−1.5 s for preparing continuous Pt films by ALD. These conditions have become the standard used by other groups.[4,5,15] This temperature is considered to be the upper limit before the $MeCpPtMe_3$ begins to decompose. During thermal decomposition, the Pt film grows rapidly and is contaminated with residual carbon.[13] Thermal decomposition must be avoided because it prohibits the self-limiting growth mechanism in ALD. Aaltonen and co-workers[7] observed that, at a lower temperature, that is, 250 °C, Pt ALD with air only produces very thin films. However, the rate-limiting step for Pt ALD at lower temperatures is most likely the Pt oxidation because Pt films can be formed easily at 100−200 °C by an O_2 plasma treatment, or O_2 plasma treatment followed H_2 reduction. We find that decomposition of $MeCpPtMe_2$ adsorbed at lower temperatures can be exploited to prepare highly loaded, uniformly sized 1−2 nm Pt nanoparticles.

After low-temperature adsorption of $MeCpPtMe_3$ on the oxide supports, decomposition occurs at 300 °C in air, 200 °C in H_2, and 300 °C in N_2. Therefore, to form Pt nanoparticles by ALD, the temperature should be lower than the precursor decomposition temperature. To ensure that the Pt is uniformly deposited on the entire support, long adsorption times were also chosen. The surface area and porosity of the support will determine the exposure time for full coverage.[24] The normalized surface loading (Figure 3b) for higher surface area γ-Al_2O_3 (350 m^2/g) indicates that 30 min was insufficient for saturation coverage. For Pt on alumina, saturation coverage was obtained in about 2 h. For lower surface area supports of TiO_2 (220 m^2/g) and $SrTiO_3$ (20 m^2/g), approximately 30 min is sufficient for saturation coverage.

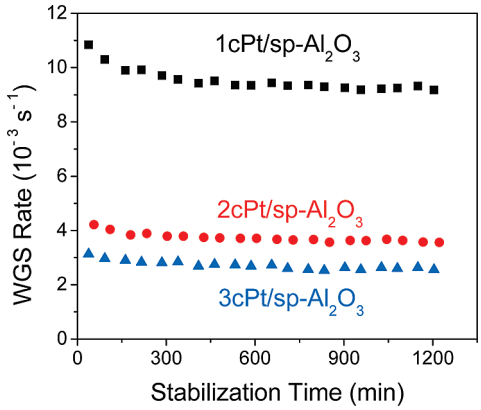

Figure 9. Stability of Pt ALD catalysts (constant temperature and inlet concentrations). WGS rate expressed as moles of CO reacted per mole of total Pt and calculated at 295 °C and 1 atm (6.8% CO, 21.9% H_2O, 8.5% CO_2, 37.4% H_2).

Whereas low-temperature $MeCpPtMe_3$ leads to 1−2 nm Pt nanoparticles, long exposure times at high temperature leads to the formation of large Pt particles. Pt deposition at 300 °C, for example, for 30 min with the long deposition times leads to thermal decomposition of $MeCpPtMe_3$ and metallic films, not formation of nanoparticles. At 300 °C, a metallic Pt film was visible throughout the heated section in the reactor, including on the oxide supports, sample holder, and quartz reactor tube. Characterization of the sample by XANES and EXAFS clearly indicated that the deposited material was bulk metallic Pt with the coordination number of 11 and Pt−Pt bond distance of 2.77 Å. Therefore, 300 °C with long exposure times is not optimal for Pt nanoparticle formation. Although prolonged $MeCpPtMe_3$ adsorption is not suitable, short adsorption times from a few seconds to several minutes does produce uniform nanoparticles; however, in general, these are slightly larger than those prepared at lower temperatures (Figure 8a−c). Thus, by changing the temperature and exposure times, one can prepare uniform-sized 1−2 nm particles at low temperature and slightly larger 2−3 nm particles at higher temperature. Because many catalytic reactions are particle-size-dependent, the ability to control the particle size precisely will allow these effects to be studied in detail.

4.2. $MeCpPtMe_3$ Adsorption and Treatment on Oxide Supports. The adsorption mechanism for $MeCpPtMe_3$ onto the oxide supports will affect the Pt nanoparticle formation. One adsorption mechanism for organometallic precursors onto oxide supports is through chemisorption to surface hydroxyl groups (eq 3) (see ref 25 and references therein). As shown in eq 3, E represents the support (with hydroxyl groups), M the metal atom, and R the organic ligand.

$$(E{-}OH)_n + MR_x \rightarrow (E{-}O)_nMR_{x-n} + nRH \qquad (3)$$

In support of this model, Yermakov[25] observed a decrease in the SiO_2 3740 cm^{-1} hydroxyl group intensity upon adsorption of group VIII π-allyl compounds. Kessels and co-workers[15] also found evidence for the reaction of $MeCpPtMe_3$ with surface hydroxyl groups using FTIR measurements. Their findings were consistent with the release of one methyl ligand per $MeCpPtMe_3$ molecule upon adsorption. In contrast, Lashdaf and co-workers[26] suggested that three methyl groups from $MeCpPtMe_3$ react with alumina and silica surfaces, forming methane and chemisorbed −O−Pt(MeCp). This suggestion was based on the observations that Pt assumed the 2+ oxidation state, according to X-ray photoelectron spectroscopy (XPS), and that the ratio of carbon to Pt^{2+} was 6, as determined by LECO carbon analysis. The Pt^{2+}oxidation state implies a partial reduction of the adsorbed precursor during chemisorption.[26] After the adsorbed precursor on Al_2O_3 was decomposed at 100 °C, XPS indicated a mixture of Pt^0 (56%) and Pt^{2+} (44%). In our study, the XANES and EXAFS spectra reveal that the adsorbed Pt precursor has a structure similar to that of the initial $MeCpPtMe_3$ precursor (prior to adsorption) and the oxidation state is unchanged, that is, Pt^{4+}. Furthermore, we find a less than 10% reduction to Pt^0 on γ-Al_2O_3 after the precursor adsorption (Table 1 and Table 2, first cycle). Consequently, we propose a structure for the adsorbed precursor (Figure 4c, (I)) similar to that of Kessels.[15] To summarize, $MeCpPtMe_3$ reacts with the support hydroxyl groups, releasing one methyl ligand (and forming CH_4, which was not quantified in this study) and resulting in atomically dispersed, chemisorbed $MeCpPtMe_2$.

During the $MeCpPtMe_3$ exposures, chemisorption continues until the oxide surface is fully saturated. At least up to four Pt ALD cycles, the amount of Pt deposited onto the support is the same, irrespective of the post-treatment gas or amount of preadsorbed Pt. The type of oxide support had little effect on the adsorption and reaction of $MeCpPtMe_3$. XANES spectra and fitting results for adsorbed $MeCpPtMe_2$ on γ-Al_2O_3, TiO_2, and $SrTiO_3$ were very similar (Tables 1 and 2). The maximum amount of adsorbed Pt, on the other hand, does depend on the support and was found to be proportional to the support surface area.

4.3. Effect of Treatment Gas. Either H_2 or O_2 can be used to effectively reduce or oxidize the adsorbed $MeCpPtMe_2$ on the support. The results during the treatment process and the interaction between Pt precursor and the reduced or oxidized surface during subsequent ALD cycles are discussed below.

4.3.1. H_2 Treatment. Hydrogen was used as a post-treatment gas to reduce the adsorbed precursor to 1−2 nm metallic nanoparticles. During reduction, the organic ligands quickly decomposed (possibly to methane and methylcyclopentane)[12] and Pt nanoparticles were formed. The proposed schemes for the metallic particle formation are illustrated in Figure 5c, (II), for the first ALD cycle and Figure 5c, (IV), for the second ALD cycle. The precursor reduction likely yields mobile Pt adatoms that aggregate to form clusters.[4,25,27] This aggregation produces clusters that are more stable because of the increased bonding energy between the surface and the clusters.[27,28] The results for H_2 reduction at 200 °C and N_2 thermal decomposition at 300 °C were similar. XANES and EXAFS revealed metallic Pt particles after thermal decomposition or reduction with similar particle sizes in the range of 1−2 nm. This was expected because, during thermal decomposition, electron-rich organic ligands can act as the reducing agent. H_2 treatment might be more advantageous to keep the Pt particles smaller relative to thermal decomposition. Because complete thermal decomposition required higher temperatures than H_2 reduction, the lower temperatures during H_2 reduction should reduce surface diffusion and limit the Pt sintering. In addition, H_2 reduction should result in fewer carbon contaminants as compared with thermal decomposition.[29]

Yermakov[25] observed that the infrared absorption features from surface hydroxyl groups increased back to the initial intensity after reduction. We believe that H_2 reduction in our experiments regenerates or uncovers hydroxyl groups on the support, allowing the chemisorption of additional $MeCpPtMe_2$ in the following ALD cycles (eq 3). The $MeCpPtMe_3$ reacts with these hydroxyl groups in subsequent ALD cycles until all

of the accessible hydroxyl groups are consumed (Figure 5b, (III and V)). The precursor adsorption and reduction cycle is speculated to continue until Pt particles completely cover the surface of the oxide support, limiting adsorption sites for the new hydroxyl groups. Although some adsorption of $MeCpPtMe_3$ may occur on the Pt particles themselves, from the XANES, we observed that, at low temperature, $MeCpPtMe_3$ is adsorbed primarily on the support and not on PtO or metallic Pt. At longer times, or as the surface coverage increases, some $MeCpPtMe_3$ does react with PtO, reducing it to metallic Pt. Although $MeCpPtMe_3$ can react on H_2-treated Pt surfaces to form continuous Pt films, at high temperature and short contact times, there appears to be little reaction of $MeCpPtMe_3$ with Pt nanoparticles at low temperature.[30]

Small, highly dispersed Pt nanoparticles are desirable for catalysis. For Pt on TiO_2 and Al_2O_3, the preparation with post-treatment in H_2 or air leads to very similar sized 1−2 nm Pt particles. Similar sizes were obtained on $SrTiO_3$ by reduction of adsorbed $MeCpPtMe_3$. TEM images of Pt on TiO_2 and $SrTiO_3$ confirm the 1−2 nm Pt particle sizes (Figure 7). The Pt particle sizes in this study are comparable to those of the Pt nanoparticles (∼1.4 nm) synthesized by Fukui and co-workers[27,28] on TiO_2(110) using $MeCpPtMe_3$. Furthermore, the density of Pt nanoparticles was observed to increase (as the ALD cycle increased to three cycles) without changes in the Pt particle size. Takakusagi and co-workers[27] also reported a similar observation for Pt MOCVD with $MeCpPtMe_3$ on TiO_2(110) by scanning tunneling microscopy (STM). They reported that the Pt particle density increased by a factor of 1.55 after the second cycle. TEM images of Pt deposited onto TiO_2 and $SrTiO_3$ also revealed small, highly dispersed Pt nanoparticles with sizes of ∼1 to 2 nm (Figure 7). These findings indicate that the Pt ALD yields a high loading of Pt nanoparticles without sacrificing the high dispersion.

4.3.2. O_2 Treatment. Pt ALD is often performed using oxygen at 300 °C to decompose the Pt precursor.[3,4,7,21,23] Consistent with these previous studies, we found that 300 °C was the minimum temperature required to completely oxidize the adsorbed Pt precursor using air. At 300 °C, the adsorbed precursor oxidation occurs too rapidly for direct monitoring by EXAFS. At 200 °C, the oxidation rate was sufficiently slow to monitor the temporal evolution of the surface species. During the first few minutes, there is a decrease in the amount of adsorbed Pt precursor and a simultaneous increase in the amount of both PtO and metallic Pt, suggesting that the adsorbed $MeCpPtMe_3$ is reduced by the organic ligand fragments during the first few minutes of the oxidation. At longer times, the metallic Pt oxidizes to PtO on the γ-Al_2O_3 support (Figure 4).

Oxidation of the adsorbed $MeCpPtMe_2$ resulted in mainly Pt(II) oxide on all three supports (i.e., TiO_2, γ-Al_2O_3, and $SrTiO_3$). The position and intensity of the XANES features for the three samples were consistent with Pt^{2+} (Table 1). Furthermore, EXAFS analysis indicated that the resulting Pt−O coordination number was approximately 4 with a bond distance of 2.04 Å for both TiO_2 and γ-Al_2O_3 (Table 4). Pt(II) oxide has a square planar structure with the corresponding coordination number of 4, whereas PtO_2 or $Na_2Pt(OH)_6$ has six Pt−O bonds.

Aaltonen[14] and Kessels[15] proposed that, during the oxygen exposures of Pt ALD, oxygen dissociates on the Pt surface to form adsorbed atomic oxygen species. Kessels et al.[15] concluded that the adsorbed oxygen coverage is approximately 0.3 ML after the O_2 treatment. At low enough pressures, 0.25 ML is the maximum coverage on a Pt(111) single crystal. See Getman et al.[31] for a more detailed account of large single-crystal Pt oxidation. The study by Kessels did not directly characterize the surface oxygen species but rather inferred them from calculations of oxygen surface coverage and quantification of the gaseous products released during the O_2 exposure. Our work directly measures the Pt surface species during the oxidation by XAFS and clearly demonstrates that PtO is formed and not chemisorbed oxygen because there is no metallic Pt; see Tables 1 and 4. Complete oxidation of Pt to the oxide at the conditions we used is well-known for Pt particles in the 1−3 nm range.[32] Thus, the state of the adsorbed oxygen during Pt ALD is different on continuous Pt films as compared with the supported Pt nanoparticles investigated in our work.

Nanoparticle reduction by thermal decomposition in N_2 or air oxidation leads to newly exposed support hydroxyl groups. During the $MeCpPtMe_3$ adsorption in subsequent ALD cycles, the Pt precursor could potentially react with either the support hydroxyl groups or the PtO. We find that, when the support surface is partially covered with PtO, $MeCpPtMe_3$ first adsorbs preferentially on the surface hydroxyls (Figure 4c, (III)). This mechanism was proposed previously for the nucleation of Pt ALD on $SrTiO_3$ surfaces.[10] Once the available hydroxyl sites are significantly decreased, one molecule of $MeCpPtMe_3$ reacts with one PtO to form one metallic Pt atom (Figure 4b, (VI)). These results are consistent with previous studies where CO, CO_2, and H_2O were detected during Pt ALD.[14,15]

On the basis of our understanding of the effect of O_2 treatment discussed above, we expect the Pt particle size to increase with increasing ALD cycles. Over sp-Al_2O_3, the Pt particle size increases steadily from 2.3 to 2.9 nm between one and three Pt ALD cycles (Figure 8). Spherical-Al_2O_3 is hydrophobic and has a lower hydroxyl density than $SrTiO_3$. In agreement with this, significantly higher Pt particle growth was observed for $SrTiO_3$ compared with the sp-Al_2O_3. Figure 6c,d shows TEM images following one and four Pt ALD cycles on $SrTiO_3$ and demonstrates that the particles grow from ∼2 to ∼6 nm. Additionally, the Pt particle density is higher for $SrTiO_3$ than sp-Al_2O_3. In previous measurements, small- and wide-angle X-ray scattering revealed that the Pt interparticle spacing and particle size on $SrTiO_3$ nanocubes decrease with increasing ALD cycles.[4] This suggested that the Pt particles coalesced, causing a decrease in the number of particles per unit area (lower dispersion). Therefore, to reduce sintering during Pt ALD, the surface hydroxyl density on the support should be reduced to provide sufficient spacing between the ALD adsorption sites.

With the higher surface area TiO_2 and γ-Al_2O_3 supports, the Pt particle size did not notably increase with increasing Pt ALD cycles, even though the supports also had PtO. The TEM images in Figure 6a,b show similar Pt particle sizes of ∼1 to 2 nm following one and four Pt ALD cycles over TiO_2. In contrast, the Pt particles were significantly larger on the lower surface area $SrTiO_3$ and sp-Al_2O_3 supports. It is possible that the 30 min $MeCpPtMe_3$ exposures were sufficient to fully saturate the sp-Al_2O_3 and $SrTiO_3$ samples, but not the γ-Al_2O_3 and TiO_2 samples. As a result, the $MeCpPtMe_3$ adsorbed on PtO in addition to surface hydroxyl groups, leading to a higher Pt loading and more particle growth. For γ-Al_2O_3 and TiO_2, the $MeCpPtMe_3$ adsorbed mainly on the hydroxyl groups, leading to a smaller increase in particle size.

This study demonstrates that ALD is an attractive catalyst synthesis method for depositing discrete Pt nanoparticles on a variety of oxide supports. The particle size, density, and dispersion could be controlled by adjusting the precursor adsorption temperature and exposure time, the number of ALD cycles, and the type of gas post-treatment. Our findings may

extend to the ALD synthesis of other noble metal nanoparticles, such as Pt, Ru, Ir, and Pd.[3,8,9,14,33] This method has several potential applications; the first is the synthesis of more uniform and varied particle sizes, as demonstrated in this study. In addition, the synthesis of bimetallic nanoparticles should also be possible.[16] For example, a second metal precursor (X) could be deposited directly onto the PtO sites to make a Pt−X nanoparticle alloy. Finally, on hydrophobic supports, such as spherical alumina, it has not been possible to prepare small Pt nanoparticles by aqueous solution methods. However, high-quality catalysts are readily prepared by ALD. These supports are especially desirable for atomic resolution TEM studies, which are not possible on other alumina supports.

4.4. Water−Gas Shift. The results from Table 5 indicate that the kinetic performance of ALD Pt/sp-Al_2O_3 catalysts is similar to that of Pt/γ-Al_2O_3 catalysts under WGS conditions. The apparent activation energies for the three Pt/sp-Al_2O_3 catalysts match the range of values reported in the literature for Pt/γ-Al_2O_3 catalysts. When compared to the typical turnover rate (TOR) of Pt/γ-Al_2O_3 catalysts with cofeeding of reaction products, the ALD Pt/sp-Al_2O_3 displays equal TORs. The TOR for the catalyst with one ALD Pt cycle supported on sp-Al_2O_3 is 2−3 times higher than the two and three cycle Pt/sp-Al_2O_3 catalysts, a small difference. These results are similar to those reported for a series of Pt/γ-Al_2O_3 catalysts studied by Panagiotopoulou and Kondarides.[34] For loadings as high as 5 wt % of Pt on an Al_2O_3 support with a surface area of 83 m^2/g, the authors concluded that weight loading and dispersion had a negligible effect on the WGS rate.

As discussed in the results of the XAFS analysis, the Pt−Pt bond distances in Table 3 were considerably smaller than those observed in bulk Pt (2.77 Å). However, the XAFS analysis of the catalysts after use in the WGS reaction resulted in Pt−Pt bond distances between 2.73 and 2.74 Å. Consequently, effects from strain in the Pt clusters are not expected to considerably influence the catalytic activity for the samples studied.

The rates for each catalyst were stable over 20 h on stream. As seen in Figure 9, the rate for each catalyst was within 80% of the initial recorded rate. Some of the deactivation can be attributed to sintering of the Pt particles. However, the changes in the average Pt particle size were ∼1 nm or less for each of the catalysts. The stability of these catalysts as well as the TOR for the WGS reaction show that the ALD preparation method results in catalysts that are kinetically similar to Pt/γ-Al_2O_3 catalysts prepared by alternate methods.

5. Conclusions

Platinum catalysts prepared by atomic layer deposition have a uniform particle size and are well-dispersed on the oxide supports. In addition, catalysts with high Pt loadings could be prepared while maintaining a small particle size. This work focused on elucidating the mechanism for Pt particle formation by monitoring the changes in the adsorbed Pt species by XAFS. The $MeCpPtMe_3$ chemisorbs on surface hydroxyl groups. Pt nanoparticles were formed by either H_2 reduction at 200 °C or thermal decomposition at 300 °C. Air post-treatment of the nanoparticles at 300 °C leads to complete oxidation and the formation of PtO. In the subsequent ALD cycles, $MeCpPtMe_3$ preferentially adsorbs on the support hydroxyl groups rather than on PtO. However, as the number of support sites decreases, $MeCpPtMe_3$ reacts with PtO, forming metallic Pt. One $MeCpPtMe_3$ reduces one PtO, forming one metallic Pt atom.

Lower temperatures and longer adsorption times lead to 1−2 nm Pt particles. Adsorption of $MeCpPtMe_3$ at 300 °C using shorter exposure times gives 2−3 nm particles, and at a high surface density, $MeCpPtMe_3$ reacts with PtO, leading to particles as large as ∼5 nm. Under each set of synthesis conditions, the particles are fairly uniform in size and evenly distributed on the support. The ALD Pt catalysts exhibit excellent catalytic activity and stable WGS reaction rates that are comparable to those of conventional incipient wetness impregnation catalysts. Synthesis of metal nanoparticles by ALD has several potential applications where uniform sizes, novel metal compositions, TEM studies, or small alloy particles are required.

Acknowledgment. This work is supported by the U.S. Department of Energy, Office of Basic Energy Sciences, Division of Chemical Sciences, Geosciences and Biosciences under Contract No. FWP 57703. Support from the Department of Energy, Office of Basic Energy Sciences, Chemical Sciences, under Grant No. DE-FG02-03ER15408 is also gratefully acknowledged. Use of the Advanced Photon Source was supported by the U.S. Department of Energy, Office of Science, Office of Basic Energy Sciences, under Contract No. DE-AC02-06CH11357. MRCAT operations are supported by the Department of Energy and the MRCAT member institutions.

References and Notes

(1) Bartholomew, C. H.; Farrauto, R. J. *Fundamentals of Industrial Catalytic Processes*, 2nd ed.; Wiley-Interscience: New York, 2005.
(2) Stair, P. C. *J. Chem. Phys.* **2008**, *128*, 182507.
(3) Elam, J. W.; Zinovev, A. V. V.; Pellin, M. J.; Comstock, D. J.; Hersam, M. C. *ECS Trans.* **2007**, *3*, 271.
(4) Christensen, S. T.; Elam, J. W.; Rabuffetti, F. A.; Ma, Q.; Weigand, S. J.; Lee, B.; Seifert, S.; Stair, P. C.; Poeppelmeier, K. R.; Hersam, M. C.; Bedzyk, M. J. *Small* **2009**, *5*, 750.
(5) King, J. S.; Wittstock, A.; Biener, J.; Kucheyev, S. O.; Wang, Y. M.; Baumann, T. F.; Giri, S. K.; Hamza, A. V.; Baeumer, M.; Bent, S. F. *Nano Lett.* **2008**, *8*, 2405.
(6) Liu, C.; Wang, C. C.; Kei, C. C.; Hsueh, Y. C.; Perng, T. P. *Small* **2009**, *5*, 1535.
(7) Aaltonen, T.; Ritala, M.; Sajavaara, T.; Keinonen, J.; Leskela, M. *Chem. Mater.* **2003**, *15*, 1924.
(8) Aaltonen, T.; Alen, P.; Ritala, M.; Leskela, M. *Chem. Vap. Deposition* **2003**, *9*, 45.
(9) Aaltonen, T.; Ritala, M.; Sammelselg, V.; Leskela, M. *J. Electrochem. Soc.* **2004**, *151*, G489.
(10) Christensen, S. T.; Elam, J. W.; Lee, B.; Feng, Z.; Bedzyk, M. J.; Hersam, M. C. *Chem. Mater.* **2009**, *21*, 516.
(11) Lashdaf, M.; Lahtinen, J.; Lindblad, M.; Tiitta, M.; Venalainen, T.; Osterholm, H. *Stud. Surf. Sci. Catal.* **2004**, *154*, 1708.
(12) Xue, Z. L.; Thridandam, H.; Kaesz, H. D.; Hicks, R. F. *Chem. Mater.* **1992**, *4*, 162.
(13) Hiratani, M.; Nabatame, T.; Matsui, Y.; Imagawa, K.; Kimura, S. *J. Electrochem. Soc.* **2001**, *148*, C524.
(14) Aaltonen, T.; Rahtu, A.; Ritala, M.; Leskela, M. *Electrochem. Solid-State Lett.* **2003**, *6*, C130.
(15) Kessels, W. M. M.; Knoops, H. C. M.; Dielissen, S. A. F.; Mackus, A. J. M.; van de Sanden, M. C. M. *Appl. Phys. Lett.* **2009**, *95*, 013114.
(16) Christensen, S. T.; Elam, J. W. *Chem. Mater.,* in press, **2010**.
(17) Miller, J. T.; Kropf, A. J.; Zha, Y.; Regalbuto, J. R.; Delannoy, L.; Louis, C.; Bus, E.; van Bokhoven, J. A. *J. Catal.* **2006**, *240*, 222.
(18) Rabuffetti, F. A.; Kim, H. S.; Enterkin, J. A.; Wang, Y. M.; Lanier, C. H.; Marks, L. D.; Poeppelmeier, K. R.; Stair, P. C. *Chem. Mater.* **2008**, *20*, 5628.
(19) Elam, J. W.; Groner, M. D.; George, S. M. *Rev. Sci. Instrum.* **2002**, *73*, 2981.
(20) Bollmann, L.; Ratts, J. L.; Joshi, A. M.; Williams, W. D.; Pazmino, J.; Joshi, Y. V.; Miller, J. T.; Kropf, A. J.; Delgass, W. N.; Ribeiro, F. H. *J. Catal.* **2008**, *257*, 43.
(21) Aaltonen, T.; Ritala, M.; Tung, Y. L.; Chi, Y.; Arstila, K.; Meinander, K.; Leskela, M. *J. Mater. Res.* **2004**, *19*, 3353.
(22) Bus, E.; Miller, J. T.; Kropf, A. J.; Prins, R.; van Bokhoven, J. A. *Phys. Chem. Chem. Phys.* **2006**, *8*, 3248.
(23) Aaltonen, T.; Ritala, M.; Leskela, M. *Adv. Met. Conf. 2004, Proc.* **2004**, 663.
(24) Lakomaa, E. L. *Appl. Surf. Sci.* **1994**, *75*, 185.
(25) Yermakov, Y. I. *Catal. Rev.−Sci. Eng.* **1976**, *13*, 77.
(26) Lashdaf, M.; Lahtinen, J.; Lindblad, M.; Venalainen, T.; Krause, A. O. I. *Appl. Catal., A* **2004**, *276*, 129.

(27) Takakusagi, S.; Fukui, K.; Tero, R.; Nariyuki, F.; Iwasawa, Y. *Phys. Rev. Lett.* **2003**, *91*, 066102.
(28) Fukui, K.; Takakusagi, S.; Tero, R.; Aizawa, M.; Namai, Y.; Iwasawa, Y. *Phys. Chem. Chem. Phys.* **2003**, *5*, 5349.
(29) Zinn, A.; Niemer, B.; Kaesz, H. D. *Adv. Mater. (Weinheim, Ger.)* **1992**, *4*, 375.
(30) Hoover, R. R.; Tolmachev, Y. V. *J. Electrochem. Soc.* **2009**, *156*, A37.
(31) Getman, R. B.; Schneider, W. F.; Smeltz, A. D.; Delgass, W. N.; Ribeiro, F. H. *Phys. Rev. Lett.* **2009**, *102*, 076101.
(32) Gracia, F. J.; Bollmann, L.; Wolf, E. E.; Miller, J. T.; Kropf, A. J. *J. Catal.* **2003**, *220*, 382.
(33) Silvennoinen, R. J.; Jylha, O. J. T.; Lindblad, M.; Osterholm, H.; Krause, A. O. I. *Catal. Lett.* **2007**, *114*, 135.
(34) Panagiotopoulou, P.; Kondarides, D. I. *Catal. Today* **2006**, *112*, 49.
(35) Phatak, A. A.; Koryabkina, N.; Rai, S.; Ratts, J. L.; Ruettinger, W.; Farrauto, R. J.; Blau, G. E.; Delgass, W. N.; Ribeiro, F. H. *Catal. Today* **2007**, *123*, 224.
(36) Grabow, L. C.; Gokhale, A. A.; Evans, S. T.; Dumesic, J. A.; Mavrikakis, M. *J. Phys. Chem. C* **2008**, *112*, 4608.

JP911178M